

A marine cryptochrome with an inverse photo-oligomerization mechanism

Received: 1 June 2023

Accepted: 19 October 2023

Published online: 30 October 2023

 Check for updates

Hong Ha Vu^{1,7}, Heide Behrmann^{2,7}, Maja Hanić³, Gayathri Jeyasankar², Shruthi Krishnan¹, Dennis Dannecker^{1,2}, Constantin Hammer¹, Monika Gunkel², Ilia A. Solov'yov^{3,4,5}, Eva Wolf^{1,6} ✉ & Elmar Behrmann² ✉

Cryptochromes (CRYs) are a structurally conserved but functionally diverse family of proteins that can confer unique sensory properties to organisms. In the marine bristle worm *Platynereis dumerilii*, its light receptive cryptochrome L-CRY (*PdLCry*) allows the animal to discriminate between sunlight and moonlight, an important requirement for synchronizing its lunar cycle-dependent mass spawning. Using cryo-electron microscopy, we show that in the dark, *PdLCry* adopts a dimer arrangement observed neither in plant nor insect CRYs. Intense illumination disassembles the dimer into monomers. Structural and functional data suggest a mechanistic coupling between the light-sensing flavin adenine dinucleotide chromophore, the dimer interface, and the C-terminal tail helix, with a likely involvement of the phosphate binding loop. Taken together, our work establishes *PdLCry* as a CRY protein with inverse photo-oligomerization with respect to plant CRYs, and provides molecular insights into how this protein might help discriminating the different light intensities associated with sunlight and moonlight.

Cryptochromes (CRYs) are found in both animals and plants and have evolved from DNA-repairing photolyases (PLs)¹. Animal CRYs can be subdivided into light-sensitive CRYs, namely type I (*Drosophila*-like) and type IV CRYs, and light-insensitive CRYs, namely type II (mammalian-like), CRYs². In contrast, plant CRYs appear to be exclusively light-sensitive³.

While animal and plant CRYs have evolved from different ancestral PL backgrounds⁴, they share a highly conserved PL homology region (PHR). Unlike PLs, the CRY PHR is modified by a specific C-terminal expansion (CTE), and sometimes an N-terminal expansion (NTE), postulated to dictate its biochemical function^{1,5,6}. The PHR can be structurally sub-divided into two regions, namely an N-terminal α/β -region and a C-terminal α -helical region connected by an extended

connector region. The α -helical region contains the binding pocket for the major chromophore, flavin adenine dinucleotide (FAD), which is required for the light response. In the dark resting state of type I CRYs, FAD is non-covalently bound in its oxidized form (FAD^{ox})⁷. Absorption of a blue light photon induces a photoexcited state FAD^{ox*}, which in turn abstracts an electron from a nearby tryptophan (TrpH) residue forming a radical pair between a now one-electron reduced anionic semiquinone (ASQ, FAD⁻) and a cationic tryptophanyl radical (TrpH⁺), which decays back to the ground state within minutes in the dark⁷.

The molecular mechanism behind the conversion of redox changes in FAD into an actual physiological signaling state in CRYs is still under debate. Since CRYs have no known enzymatic activity, a signaling state will most likely be defined by one or more

¹Institute of Molecular Physiology (IMP), Johannes Gutenberg-University Mainz, Hanns-Dieter-Hüsch-Weg 17, 55128 Mainz, Germany. ²University of Cologne, Faculty of Mathematics and Natural Sciences, Institute of Biochemistry, Zùlpicher Straße 47, 50674 Cologne, Germany. ³Institute of Physics, Carl von Ossietzky University of Oldenburg, Carl-von-Ossietzky Straße 9-11, 26129 Oldenburg, Germany. ⁴Research Center for Neurosensory Sciences, Carl von Ossietzky University of Oldenburg, Carl-von-Ossietzky Straße 9-11, 26111 Oldenburg, Germany. ⁵Center for Nanoscale Dynamics (CENAD), Carl von Ossietzky Universität Oldenburg, Ammerländer Heerstr. 114-118, 26129 Oldenburg, Germany. ⁶Institute of Molecular Biology (IMB), 55128 Mainz, Germany. ⁷These authors contributed equally: Hong Ha Vu, Heide Behrmann. ✉ e-mail: evawolf1@uni-mainz.de; elmar.behrmann@uni-koeln.de

conformational changes. The highly divergent CTE is a likely candidate for these^{1,4,6}. Proteolytic experiments have suggested a conformational change involving the CTE upon blue light excitation for type I^{8–10}, type IV¹¹, and plant CRYs¹². For the *Drosophila melanogaster* CRY (*DmCry*) this has been corroborated by time-resolved x-ray solution scattering experiments and molecular dynamics (MD) simulations¹³. Indeed, due to its unusually short CTE, forming only a short C-terminal tail helix (CTT, helix α 23), *DmCry* has been a focal point of attention in attempts to unravel the molecular coupling between FAD photoreduction and CTE conformational changes. FAD is not known to undergo a conformational change during photoactivation, but the photoinduced electron transfer results in a net negative charge at the flavin isoalloxazine ring. Structural data have revealed that *DmCry* His378 is positioned between the isoalloxazine ring and a so-called FFW motif at the C-terminal end of the CTT^{9,14}, similar to an active site histidine that is essential for PL DNA repair¹⁵. MD simulations suggest that the hydrogen-bonding network connecting His378, isoalloxazine ring and FFW motif is indeed sensitive to an additional negative charge on the isoalloxazine ring¹⁶, which was later confirmed by further experimental data¹⁷. The recent surge in structural data of CRYs from other species has suggested that this proposed coupling mechanism may be conserved in the CRY superfamily, albeit with lineage-specific fine-tuning, particularly for plant CRYs, since His378 is not conserved in the plant lineage and their most stable FAD form is a one-electron reduced neutral semiquinone (NSQ, FADH[•]). Interestingly, while it is widely accepted that blue light-activated plant CRYs oligomerize and that this is important for downstream signaling¹⁸, signaling by non-plant CRYs is largely thought to depend on the conformation of the CTE in the CRY monomer¹⁹. There are currently two known exceptions to this dogma: Firstly, dark state dimers have been reported for the animal-like CRY from the algae *Chlamydomonas reinhardtii* (*CraCry*)²⁰, although this could not be reproduced in later experiments²¹. Secondly, for the photoactive L-CRY from the bristle worm *Platynereis dumerilii* (*PdLCry*), dimers were observed in in vitro assays using SEC-MALS and proposed to be of physiological importance²².

PdLCry is one of two light-sensitive CRYs identified in this marine invertebrate, which is an important model system for both genetic and molecular studies²³. Genetic and behavioral experiments have identified *PdLCry* as an important timekeeper of its lunar-circle dependent

spawning behavior^{22,24}. Both in vivo and in vitro data revealed a peculiar light-sensitivity that allows *PdLCry* to respond to dim moonlight^{22,24}.

Here, we solve the structure of both dark state and blue light-illuminated *PdLCry* using cryo-electron microscopy (cryo-EM) in combination with single-particle reconstruction techniques. Our dark state structure reveals a distinct dimerization interface centered on helix α 8, while the blue light-illuminated structure shows that *PdLCry* monomerizes upon intense illumination. Furthermore, our structural analysis together with functional data suggest the phosphate binding loop (PBL) as a central element for the molecular coupling between the chromophore, the CTT and the dimer interface. Together, our study uncovers a mechanism of light-induced inverse oligomerization, which has important implications for our understanding of the ability of *PdLCry* to discriminate moon- from sunlight.

Results

PdLCry features subtle but distinct sequence differences separating it from classical type I CRYs

As a first step to decipher why *PdLCry* is able to dimerize, we performed an evolutionary analysis of its sequence. This analysis confirmed the previous association of *PdLCry* with type I CRYs²⁵. However, we find that *PdLCry* is distinctly separated from classical members of this lineage (Fig. 1a). Indeed, a detailed alignment of *PdLCry* with the only type I CRY with a known structure to date, *DmCry*^{9,14}, reveals subtle but distinct sequence differences in regions reported to be important for the molecular properties of *DmCry*: *PdLCry* has a shortened protrusion loop, an FCW sequence instead of an FFW sequence at the CTT, and a tyrosine in the sulfur loop (Fig. 1b, Supplementary Fig. 1, Supplementary Table 1). However, even a close comparison of their sequences did not provide a molecular explanation for the different oligomeric states of the two proteins. Therefore, we set out to elucidate the molecular architecture of *PdLCry* using molecular cryo-electron microscopy (cryo-EM).

PdLCry forms a dimer in the dark state featuring a distinct dimer interface

PdLCry was heterologously expressed in *Sf9* insect cells and purified under far-red light conditions (Supplementary Fig. 6a) to ensure that

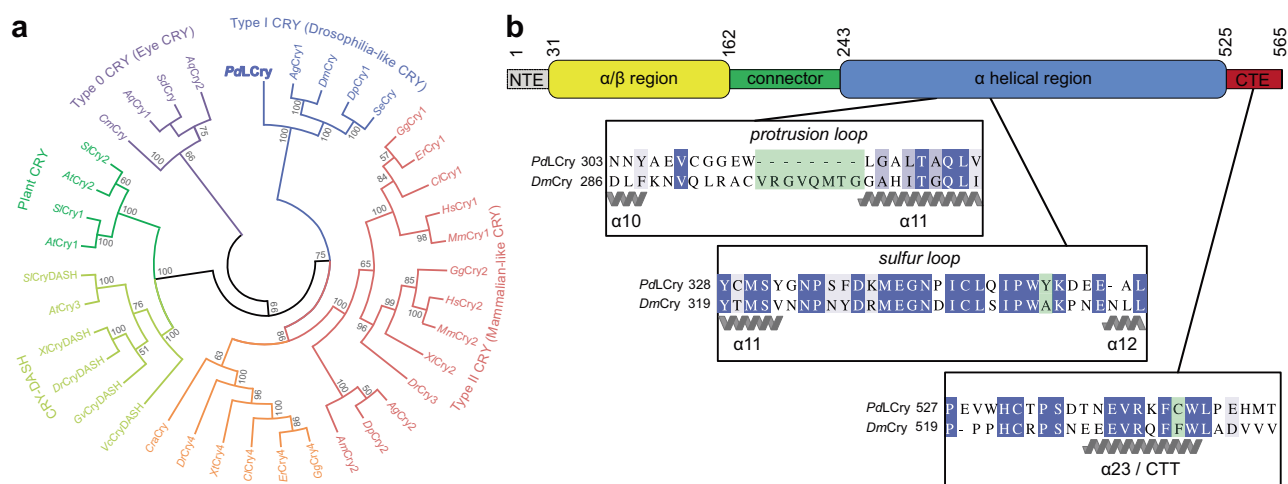


Fig. 1 | *PdLCry* belongs to the type I CRY lineage but has unique sequence features. **a** Evolutionary analysis of the CRY family using a maximum likelihood approach shows that *PdLCry* belongs to the type I CRY lineage (blue), but forms a subbranch of this lineage. Small numbers indicate the bootstrap support of the branch association. Full species names and protein sequences used are listed in Supplementary Table 1. **b** Cartoon representation of the domain composition of

PdLCry. Small numbers indicate the residue at the region boundary. Inserts show excerpts from a sequence alignment to *DmCry*, highlighting differences (marked green) in the protrusion loop, the sulfur loop and the C-terminal tail helix (CTT) FFW motif. See Supplementary Fig. 1 for the complete sequence alignment. Secondary structure annotation (α -helix indicated in gray) has been published in⁹.

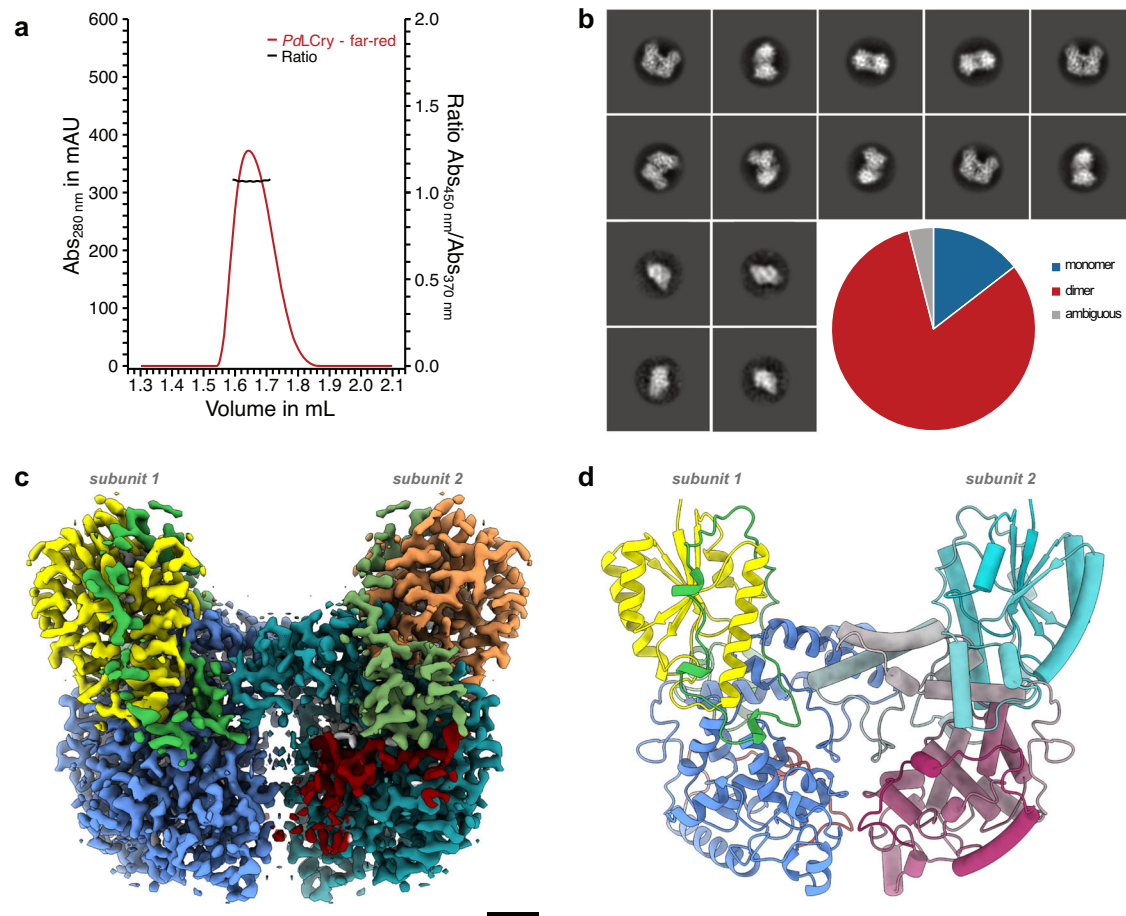


Fig. 2 | FAD^{ox}-bound PdLCry forms a unique dimer in the dark state. **a** Analytical size exclusion chromatography of PdLCry using a Superdex 200 Increase 5/150 GL column under far-red light conditions shows a slightly tailing elution peak following absorption at 280 nm (red curve), likely corresponding to a dimeric state of the protein. The nearly equal absorbance at 370 nm and 450 nm (black line; $Abs_{450nm}/Abs_{370nm} = 1.06$) confirms that PdLCry was successfully maintained in the FAD^{ox} bound dark state²⁶. **b** Representative 2D class averages of an unsupervised 2D classification of the dark state PdLCry cryo-EM sample show predominantly dimeric particles, with few monomeric particles. Quantification of all protein-shaped particles suggests that approximately 80% of the protein is present as a dimer after

vitrication under far-red light conditions. **c** Surface representation of the cryo-EM density map of PdLCry shows a butterfly-shaped dimer, with a large interaction interface formed by the α -helical region (blue) with contributions from the connector region (green). Subunit 2 is shown in darker shades. In the shown orientation, the CTE is only visible for subunit 2 (dark red). Scale bar corresponds to 10 Å. **d** Atomic model built into the cryo-EM density map shows that PdLCry adopts the typical PL/CRY fold and that both subunits are arranged in parallel. Subunit 1 is shown in cartoon style using a coloring scheme identical to that used for subunit 1 in panel (c). Subunit 2 is shown in a pipes-and-planks style using a color gradient from cyan (N-terminus) to maroon (C-terminus).

FAD remained in its oxidized ground state (FAD^{ox}) as previously described²². As for Poehn et al., PdLCry purified as a homodimer under these conditions with an absorbance ratio of 450 nm to 370 nm of 1.06 (Fig. 2a), indicating an FAD^{ox} loaded protein²⁶. The purified protein was vitrified in liquid ethane under far-red light conditions to produce cryo-EM grids of the dark state. Data acquisition and unsupervised 2D classification indeed revealed predominantly dimeric particles with a small fraction of putative monomers (Fig. 2b). We were able to refine the subset of particles composed of two subunits to obtain a dimeric structure with the PdLCry subunits arranged in parallel. As we did not observe any asymmetry during the reconstruction procedure, we enforced C2 symmetry in later reconstruction stages, yielding a final cryo-EM density map at 2.6 Å resolution (Fig. 2c, Supplementary Fig. 2). The exquisite resolution of the final, C2 symmetric 3D map allowed us to build an almost complete atomic model of PdLCry (Fig. 2d, Supplementary Table 2). We observe a near stoichiometric occupancy of the ligand FAD, but no density for additional antenna chromophores or other nucleotides. Our map shows an overall fold reminiscent of that observed in other type I CRYs, with an N-terminal α/β region (31–161) and a C-terminal α -helical region (243–524) connected by a largely well-resolved connector (162–242). While we do not observe density for

the PdLCry specific NTE (1–30), the PdLCry specific CTE (526–565) is largely well resolved and features a well-resolved C-terminal tail helix (CTT, 537–544), which resembles the helix observed in DmCry^{9,14}. The density for the last nine C-terminal residues (557–565) was strongly fragmented, suggesting considerable flexibility. The arrangement of the subunits in the dimer does not resemble either that of plant CRYs, nor that of the crystal dimer arrangement of DmCry (Supplementary Fig. 3a, b). Instead, the dimer interface in PdLCry is predominantly formed by the N-terminal part of the α -helical region with some contribution from the connector region. Molecular dynamics simulations show that the solvent-accessible surface area buried in the interface is comparable to that of the biologically relevant AtCry2 dimer, despite its different arrangement (Supplementary Fig. 3c–e).

The main dimer interface is formed between helices $\alpha 8$ of both subunits, with helices $\alpha 8$ running antiparallel at an angle of 42 degrees, flanked by interactions mediated by the connector region and the PBL (Fig. 3a, b). While helix $\alpha 8$ and the flanking regions adopt a fold that overlaps well with available structures of DmCry, the archetypal type I CRY, several key residues differ (Fig. 3c): the positions of Thr253 and Thr260 in PdLCry are occupied by bulkier amino acids in DmCry, namely Glu236 and His243, which would likely clash in a similar dimer

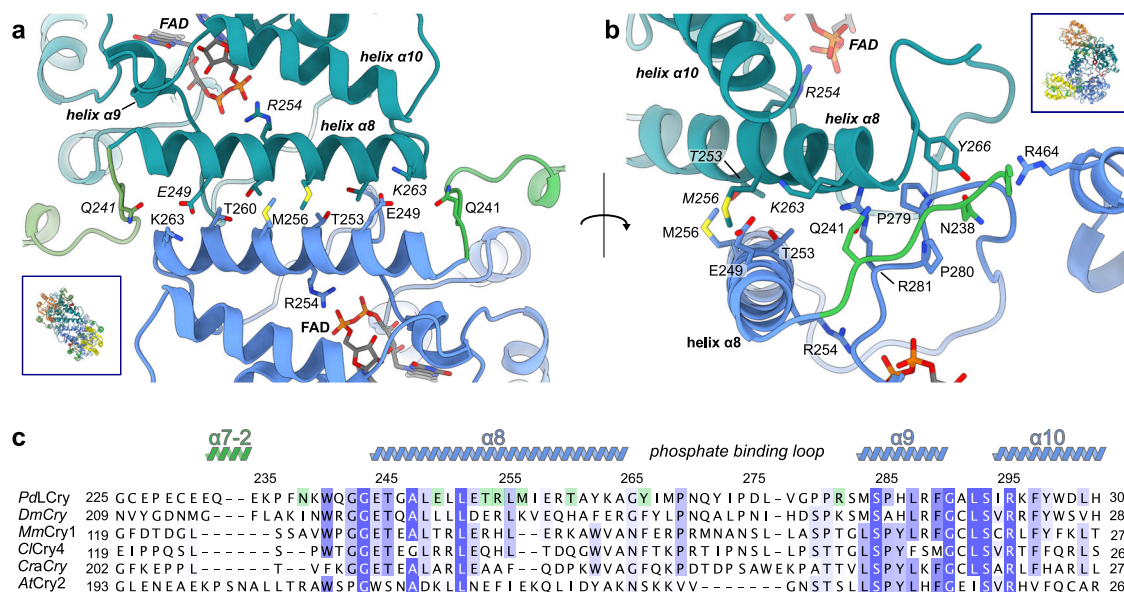


Fig. 3 | Helix $\alpha 8$ and its flanking regions are central to the dimer interface.

a Close-up view of the dimer interface and **b** 90-degree rotated view highlight the importance of helix $\alpha 8$ for the dark state dimer. Helix $\alpha 8$ of subunit 1 (using the same color code as in Fig. 2) runs antiparallel to helix $\alpha 8$ of subunit 2 (colored in darker shades as in Fig. 2), at an angle of 42 degrees. The contact point between the two helices is at the central Met256, flanked by Thr253 and Thr260. Glu249 and Arg281 appear to lock the helices in place, with possible additional stabilization by interactions centered around Tyr266 of the phosphate binding loop. Arg254 of

helix $\alpha 8$ contacts the FAD chromophore. Inserts show the respective orientation of the dimer in **(a)** and **(b)**. **c** Sequence alignment of *PdLcry* with plant, animal and animal-like CRYs of known structure indicates that the observed dimer interface is unique to *PdLcry*. Residues discussed in the text are highlighted in green. Secondary structure elements and amino acid numbering of *PdLcry* are shown above the sequences. Full species names and protein sequences used are listed in Supplementary Table 1.

arrangement. Similarly, the position of the central Met256 is occupied by a bulkier lysine (Lys239), and the position of Glu249 is occupied by a non-polar leucine residue (Leu232) in *DmCry*. Apart from the differences in helix $\alpha 8$, we note unique dimer interactions involving Tyr266 of the PBL, especially with Pro279 (PBL) and Asn238 (connector) from the other subunit. These interactions are not possible in *DmCry* because Tyr266 is replaced by a phenylalanine (Phe249), which appears to be conserved in other animal and animal-like CRYs (Fig. 3c). In addition, the position of Asn238 is occupied by a non-polar isoleucine (Ile221) in *DmCry*. Indeed, MD simulations confirm the importance of Asn238, Glu249, and Tyr266 as key residues that, due to their polar side chains, stabilize the dimer interface through hydrogen bond formation. (Supplementary Fig. 3f).

Structural elements highlight a molecular connection between the chromophore FAD, the CTT, and the dimer interface

A chain of four tryptophan residues, comprising Trp_A428, Trp_B405, Trp_C351, and Trp_D402, lines the path from the FAD to the protein surface and occupies identical positions as observed in the archetypical type I CRY *DmCry* (Fig. 4a, b). However, the sulfur loop of *PdLcry* has an additional surface-exposed Tyr352 that occupies a position similar to the terminal tyrosine in the type IV CRY *ClCry4*¹¹ (Fig. 4b). In *ClCry4*, this terminal tyrosine (Tyr319) has been shown to increase the lifetime of the radical state¹¹, as also observed for the terminal tyrosine residue that replaces Trp_D in *CraCry*²⁰. To test whether this terminal tyrosine does indeed affect the efficiency of FAD photoreduction in *PdLcry*, we replaced Tyr352 with either an alanine or an aspartate as found in *DmCry* and *CraCry* (Fig. 4b, Supplementary Fig. 1). Both *PdLcry*^{Y352A} and *PdLcry*^{Y352D} form dimers in the dark (Supplementary Fig. 6i, j), but both mutations lead to a less efficient FAD photoreduction under illumination conditions mimicking naturalistic sunlight conditions at the habitat of *P. dumerilii*²². Indeed, for both mutations photoreduction was slower and incomplete after 20 min sunlight illumination (Supplementary Fig 4a, b), different from

wildtype *PdLcry* that is almost completely photoreduced using identical conditions (Supplementary Fig. 4c).

In the dark state, the CTE is anchored in the vicinity of the FAD binding site by a CTT comprising residues 537 to 545. This CTT occupies an identical PL-DNA substrate binding pocket as in *DmCry*⁹ (Fig. 4c). Interestingly, Cys544 of the FCW motif in *PdLcry* adopts a conformation similar to Phe535 of the FFW motif in *DmCry* and, despite being less bulky, binds into an almost identical hydrophobic pocket delineated by Val431, Leu440, Val540 and Phe446, the latter occupying a similar position to *DmCry* Val437 (Fig. 4c). Notably, the smaller size of the cysteine side chain compared to the phenylalanine side chain allows His390 of helix $\alpha 14$ to adopt a different conformation compared to the corresponding Asn382 in *DmCry* (Supplementary Fig. 4d). Avian type IV CRYs¹¹ and the animal-like *CraCry*²⁷ also have a histidine at this position instead of an asparagine, but in a rotamer superimposed on Asn382 in *DmCry* (Supplementary Fig. 4d). Compared to *PdLcry*, this different histidine rotamer could possibly be due to the absence of a CTE in the truncated constructs used for crystallography.

As for *DmCry*, Trp545 in *PdLcry* is positioned at the end of the CTT. His386 (corresponding to *DmCry* His378) and the PBL residues Pro274 (corresponding to *DmCry* Pro257) and Gln271 delineate the binding pocket of Trp545. Thereby, the FCW motif in *PdLcry* is coupled to the dimer interface through the PBL. Interestingly, Gln271 is residing in a similar position as *DmCry* Arg298 from the protrusion loop, which is considerably shorter in *PdLcry* compared to *DmCry* (Fig. 4c). In *DmCry* Arg298 has been implicated in stabilizing the dark state by anchoring *DmCry* Trp536^{9,28}, suggesting that Gln271 could play a similar role in *PdLcry*.

Phe543 occupies an identical position to *DmCry* Phe534 and is similarly delineated by Trp430 (*DmCry* Trp422) and His386 (*DmCry* His378). Unlike in *DmCry*, the CTE is additionally stabilized by a cation- π interaction between Trp530 from the CTE and Arg174 from the connector region (Supplementary Fig. 4e), which is neither possible in

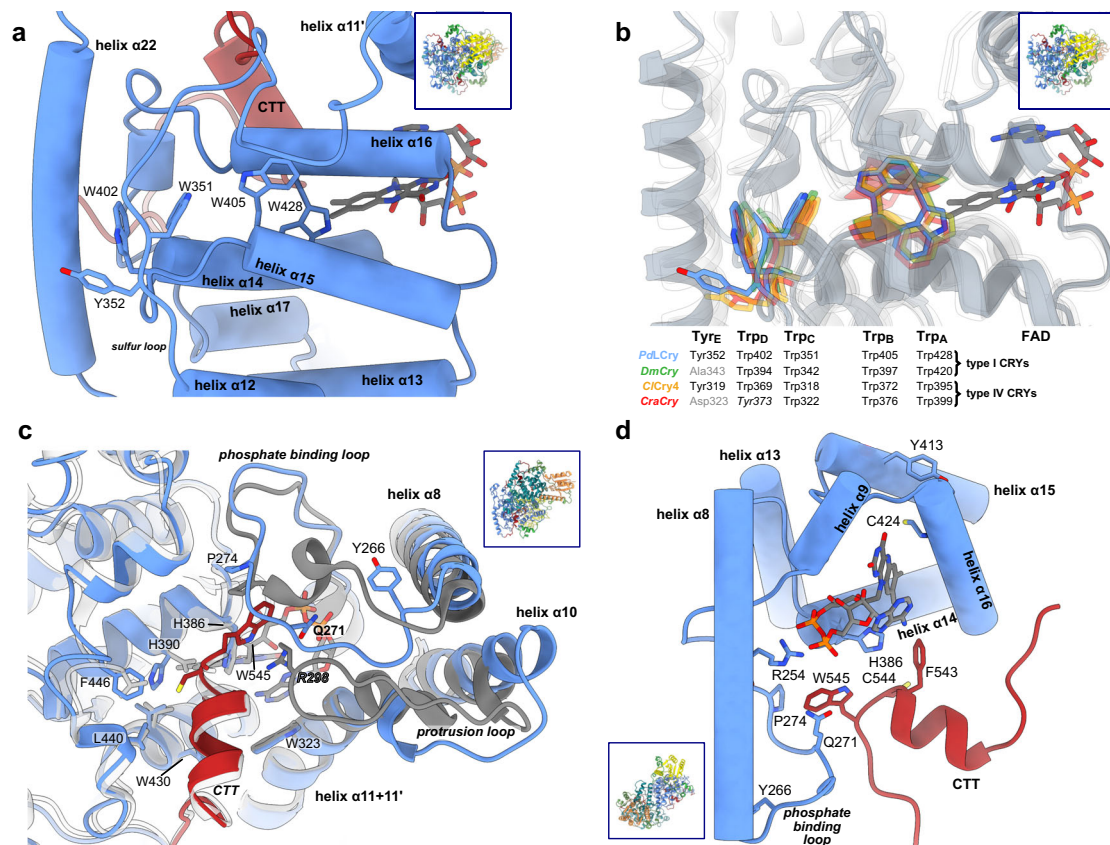


Fig. 4 | Structural data suggest that the PBL links chromophore activation, dimerization and the CTT release. **a** *PdLCry* has five aromatic residues potentially involved in the photoinduced electron transfer, namely Trp428 (Trp_A), Trp405 (Trp_B), Trp351 (Trp_C), Trp402 (Trp_D) and Tyr352 (Tyr_E). **b** The core Trp-triad consisting of Trp_A, Trp_B, and Trp_C is conserved in the light-responsive type I and IV CRYs whose structure has been solved to date: *PdLCry* (blue), *DmCry* (green; PDB 4JZY), *ClCry4* (orange; PDB 6PU0), and *CraCry* (red; PDB 6ZM0). The fourth aromatic residue, which extends this to a Trp-tetrad, is conserved except for *CraCry*, which features a tyrosine at this position. Only *PdLCry* and the type IV CRY *ClCry4* further extend the electron transport chain by a fifth member, which is a tyrosine in both proteins. *PdLCry* is shown in transparent gray, the other CRY structures are shown in transparent white. **c** An overlay of the *PdLCry* (colored) and the *DmCry* (gray and white; PDB 6WTB) structures shows that both share a CTT that is anchored in the DNA substrate binding pocket of PLs. However, instead of an FFW motif, the *PdLCry* CTT is anchored by an FCW motif. The smaller Cys544 interacts

with His390, which occupies a different position compared to *DmCry* Asn382. Importantly, the *PdLCry* protrusion loop is considerably shorter than its wild-type *DmCry* counterpart (dark gray). This results in a different contact to the FCW motif: whereas in *DmCry* Arg298 (gray) from the protrusion loop contacts the CTT tryptophan residue, in *PdLCry* this stabilizing contact is mediated by Gln271 from the phosphate binding loop, which also harbors Tyr266. Therefore, in *PdLCry* the CTT is structurally linked with the dimer interface helix $\alpha 8$, rather than with the helices $\alpha 10$ and $\alpha 11$ as observed in *DmCry*. **d** FAD is bound in a typical type I CRY FAD-binding site, with Cys424 contacting the N5 position of the isoalloxazine ring of FAD, and Tyr413 blocking solvent access to FAD. Our dark state structure reveals a molecular network surrounding FAD and connecting it to both the CTT and the dimer interface helix $\alpha 8$. His386 is positioned between FAD and the FCW motif, while Gln271 from the phosphate binding loop connects helix $\alpha 8$ to Trp545 of the CTT-anchoring FCW motif, and Arg254 connects this helix to the chromophore. Inserts show the orientation of the dimer for each panel.

DmCry nor *ClCry4* as the corresponding residues are Pro521 and Ile153, and Arg497 and Ser146 respectively. C-terminal to the CTT, the remaining CTE passes through a cleft defined by both subunits of the dimer, although the more fragmented density in this region implies conformational flexibility.

The FAD chromophore bound adjacent to the CTT is stabilized by a binding pocket defined primarily by residues from helices $\alpha 9$, $\alpha 14$, and $\alpha 16$, the PBL and the $\alpha 15$ - $\alpha 16$ loop (Fig. 4c, d). As in other type I CRYs, the N5-interacting residue is a cysteine, namely Cys424 (*DmCry* Cys416), which has been proposed to disfavor the conversion to the two-electron reduced NSQ state of the chromophore FAD^{9,14,29}. Solvent access to the FAD binding site⁷ could be blocked by Tyr413, which occupies an equivalent position as Leu405 in *DmCry*. As reported for *DmCry*^{16,17}, His386 (*DmCry* His378) bridges the FAD chromophore to the FCW motif of the CTT and is thus in a suitable position to allow the electronic state of the isoalloxazine ring to be transmitted to the CTE.

Interestingly, in addition to the Gln271-mediated coupling between helix $\alpha 8$ and the CTT, the dimer interface helix $\alpha 8$ is also directly coupled to the FAD via Arg254, which is located at the center

of helix $\alpha 8$ (Fig. 4d). We therefore asked ourselves whether there is a mechanistic coupling between the redox state of FAD, the CTE and the oligomeric state of *PdLCry*.

Activation of *PdLCry* by intense blue light disrupts the dimer

To test whether *PdLCry* does indeed respond to blue light by changing its oligomeric state, we performed size-exclusion chromatography (SEC) under continuous and intense blue light irradiation. In comparison with the elution pattern observed under far-red light conditions, we observe a shifted elution peak, likely corresponding to monomeric *PdLCry*, with an absorbance ratio of 450 nm to 370 nm of 0.28, suggesting an ASQ-loaded protein (Fig. 5a). *PdLCry* had previously been shown to revert to the ground state within minutes²². Therefore, cryo-EM samples were vitrified in liquid ethane within less than 5 s after intense blue light irradiation. Data acquisition and unsupervised 2D classification using identical conditions as for the dark state dataset indeed revealed almost exclusively monomeric particles (Fig. 5b). Unfortunately, the low molecular mass combined with a strong preferential orientation of the particles on the grid precluded us from

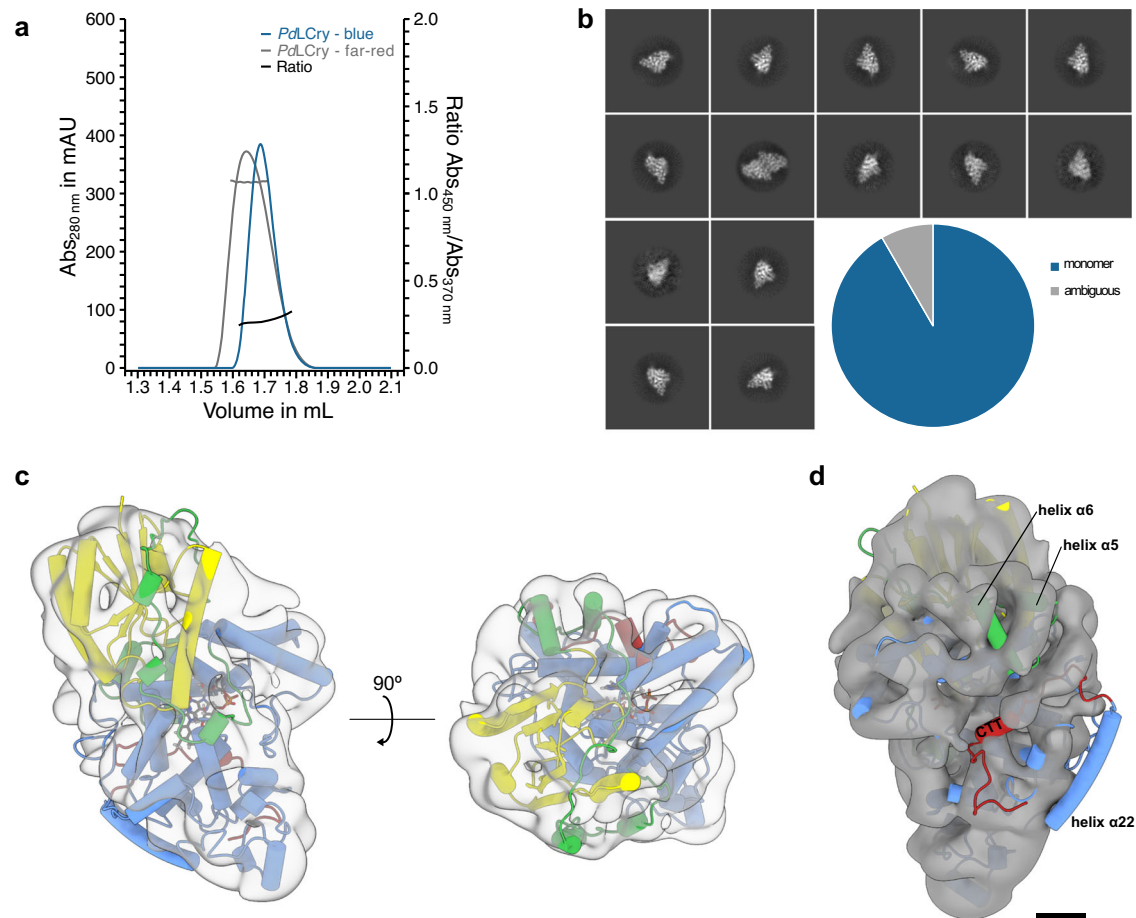


Fig. 5 | Under intense illumination FAD^{ASO}-bound PdLCry disassembles into a monomer. **a** Analytical size exclusion chromatography using a Superdex 200 Increase 5/150 GL column of PdLCry under continuous blue light conditions shows an elution peak following absorption at 280 nm (blue curve), which, based on comparison with the elution profile of the dark state SEC (gray curve), likely corresponds to a monomeric state of the protein. The dominant absorption at 370 nm compared to 450 nm ($Abs_{450nm}/Abs_{370nm} = 0.28$) suggests that PdLCry was maintained in the FAD^{ASO}-bound photoactivated state, in which the anionic semiquinone radical shifts the spectral properties of FAD²⁶. **b** Representative 2D class averages of an unsupervised 2D classification of the photoactivated PdLCry cryo-EM sample confirm the absence of dimeric particles after illumination.

Quantification of all protein-shaped particles implies that at least 90% of the protein is monomeric. Only a few classes are ambiguous, showing two subunits but in an unusual arrangement, possibly due to the close packing of the particles on the cryo-EM grid. **c** Surface representation of the cryo-EM density map of photoactivated PdLCry low-pass filtered to 8 Å shows a classical PL/CRY-shaped monomer. Due to the limited data quality, we refrained from building an atomic model. However, a single subunit of the dark state PdLCry structure (using the same colors as in Fig. 2) fits well with the observed density. **d** Apart from helix $\alpha 22$, for which there is no clear density, parts of the connector region, especially helices $\alpha 5$ and $\alpha 6$, appear to adopt a different conformation, and the density for the CTT and C-terminal parts of the C-terminal expansion is largely fragmented. Scale bar corresponds to 10 Å.

obtaining a high-resolution reconstruction (Supplementary Fig. 5). Due to the limited resolution and strong anisotropy of the 3D cryo-EM map, we refrained from building an atomic model for the activated state. Nevertheless, rigid body fitting of a single subunit from our dark state atomic model into the monomeric 3D map reveals a general fit (Fig. 5c), however with poorer fits for helix $\alpha 22$ and the CTT (Fig. 5d). Both elements have previously been suggested to become more mobile upon blue light activation for other CRY proteins^{13,21}.

Mutagenesis highlights the role of helix $\alpha 8$, the PBL and the CTT in PdLCry dimer formation

To identify the structural elements that control the oligomeric state of PdLCry, we introduced selected amino acid mutations and investigated the oligomeric state of the mutant proteins by performing SEC under far-red light conditions. First, we investigated direct mutations of the dimer interface helix $\alpha 8$. To study the effect of steric clashes, we introduced a bulky side chain into helix $\alpha 8$ by replacing Thr253 of helix $\alpha 8$ with an arginine. Indeed, this shifts the elution volume of PdLCry^{T253R} towards lower mass (Fig. 6a, Supplementary Fig. 6b). Similarly, introducing a charge reversal by replacing Glu249 of helix $\alpha 8$

with an arginine shifts the elution volume of PdLCry^{E249R} towards lower mass (Fig. 6a, Supplementary Fig. 6c). Combining both T253R and E249R as a double mutation in PdLCry^{E249R,T253R} shifts the SEC elution volume to the same volume as observed for the PdLCry^{E249R} and PdLCry^{T253R} proteins (Fig. 7a, Supplementary Fig. 6d). Comparing the elution volumes of PdLCry^{T253R}, PdLCry^{E249R} and PdLCry^{E249R,T253R} with the elution profile of wildtype PdLCry, we note that the elution peak of the mutations coincides with a shoulder in the elution profile of wildtype PdLCry. Since we observed a subpopulation of monomeric particles in the dark state cryo-EM dataset (Fig. 2b), we assume that this shoulder peak corresponds to these monomeric particles, further corroborating that the direct interface mutations lead to a monomerization even in the dark state.

Next, based on the hypothesis that CTT undocking is a downstream effect of photoexcitation in light-sensitive CRY proteins, we investigated whether there is a functional coupling between the CTT and the oligomeric state in PdLCry. To this end, we individually mutated Phe543 and Trp545 of the FCW motif, which anchor the CTT to the PL-DNA substrate binding pocket, to alanine (Supplementary Fig. 6e, f). Indeed, both PdLCry^{F543A} and PdLCry^{W545A} elute at volumes

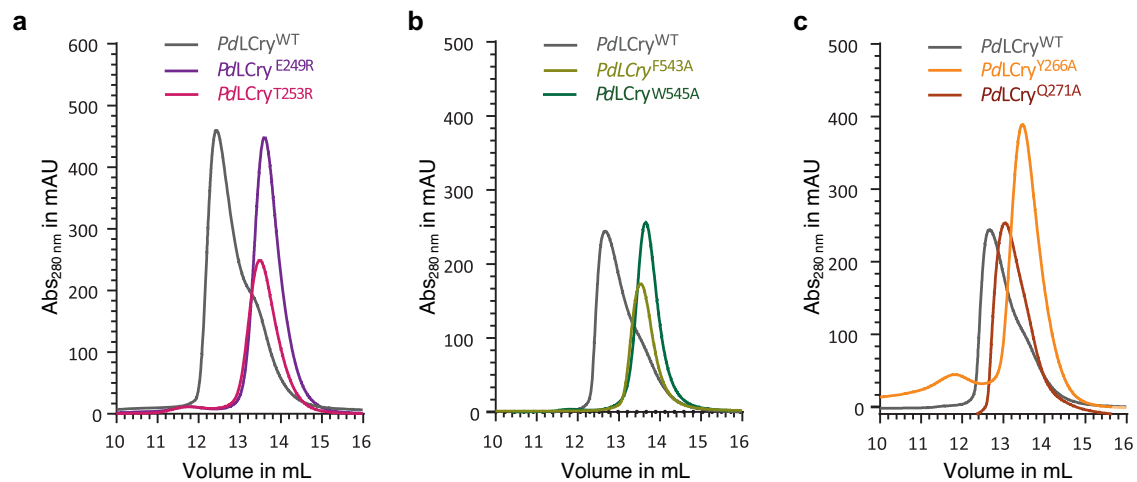


Fig. 6 | Helix α 8, the PBL, and the CTT are involved in PdLCry dimer formation.

a Analytical size exclusion chromatography of wildtype (wt) PdLCry (gray) using a Superdex 200 10/300 GL column under far-red light conditions shows a main elution peak at 12.5 mL with a significant shoulder at 13.3 mL. This shoulder suggests a partial dimer dissociation under far-red light conditions as also observed during cryo-EM (compare Fig. 2b). Using the same SEC conditions, PdLCry^{E249R} (purple) and PdLCry^{T253R} (pink), with single mutations in the dimer helix α 8, show a main elution peak coinciding with the shoulder of wildtype PdLCry (gray), suggesting that these mutations disrupt the dimer. **b** Analytical size exclusion chromatography of PdLCry^{F543A} (light green) and PdLCry^{W545A} (dark green) under far-red light conditions, with single mutations in the FCW motif anchoring the CTT, show a

main elution peak coinciding with the shoulder of wildtype PdLCry, suggesting that uncoupling the CTT from its binding pocket disrupts the dimer. **c** Analytical size exclusion chromatography of PdLCry^{Y266A} (orange) and PdLCry^{Q271A} (brown) under far-red light conditions, with single mutations in the PBL, also shows an effect on the elution profile. PdLCry^{Y266A} (orange) shows a main elution peak coinciding with the shoulder of wildtype PdLCry, consistent with a disruption of the dimer. PdLCry^{Q271A} (brown) shows an elution profile with the main peak shifted to 13 mL and a shoulder at 13.5 mL, which could suggest a partial disruption of the dimer. See Supplementary Fig. S6 for final SEC purification step of wildtype and mutant PdLCry proteins with SDS-PAGE quality control.

implying a monomer (Fig. 6b), suggesting a crosstalk of the CTT conformation to the dimer interface in PdLCry.

Our cryo-EM-derived atomic model highlights the PBL as an important structural element that is directly involved in dimer formation, via hydrogen bonds mediated by Tyr266, and connects the dimer interface to the CTT, via an interaction between Gln271 and Trp545 (Fig. 4c, d). While PdLCry^{Y266A}, in which Tyr266 of the PBL has been replaced by an alanine that cannot participate in side-chain hydrogen bonding, elutes with a volume clearly indicative of a monomer, the mutation of Gln271 to alanine has a less clear effect, and PdLCry^{Q271A} shows an elution volume between that expected for dimer and monomer (Fig. 6c, Supplementary Fig. 6g, h).

The oligomeric state of PdLCry affects the kinetics of dark recovery

Given the unique sensitivity of PdLCry compared to the archetypal monomeric type I CRY DmCry^{22,24}, and the observation that PdLCry responds to intense illumination with monomerization, we asked whether the oligomeric state of PdLCry has an influence on the properties of its photoreaction. To ensure constitutive monomer formation throughout the spectroscopic measurements, we used the combined dimer interface mutation PdLCry^{E249R,T253R} for these experiments. Based on an absorbance ratio of 450 nm to 370 nm of 1.14, which is comparable to that of the wildtype protein, PdLCry^{E249R,T253R} eluted as a monomer loaded with FAD^{OX} under far-red light conditions (Fig. 7a). Therefore, the double mutation does not appear to affect the ground state of the FAD chromophore. Under continuous and intense blue light illumination, both wildtype PdLCry and PdLCry^{E249R,T253R} elute with almost identical volumes, further corroborating that the double mutation is indeed a monomer. Under these conditions, the absorbance ratio of 450 nm to 370 nm drops to 0.28 (Fig. 7b) for both wildtype PdLCry and PdLCry^{E249R,T253R}, suggesting that while the double mutation disrupts the dimer, it does not affect the overall ability of the chromophore in PdLCry to be photoreduced to the FAD^{ASQ}-state by blue light photons.

To analyze whether the oligomeric state affects the kinetics of PdLCry photoreduction or dark recovery, we performed time-resolved UV/Vis spectroscopy. UV/Vis spectroscopic analyses confirmed that in monomeric PdLCry^{E249R,T253R} FAD is completely photoreduced to FAD^{ASQ} after 2 min of illumination with intense blue light (41 W m⁻² at the sample), as also observed for wildtype PdLCry (Supplementary Fig. 7a). To gain insight into the photoactivation of monomeric PdLCry under sunlight conditions, we also analyzed FAD photoreduction upon illumination with naturalistic sunlight²², which has a ~9-fold lower intensity (4.6 W m⁻² at sample) than our blue light source. We found that monomeric PdLCry^{E249R,T253R}-like wildtype PdLCry - showed slower FAD photoreduction kinetics under sunlight compared to blue light, reaching the sunlight state with fully photoreduced FAD^{ASQ} within approximately 20 min (Fig. 7c, d). Moreover, the monomeric mutant showed a wildtype-like sunlight photoreduction rate (average $t_{1/2}$ wildtype = 22.7 ± 0.4 s; $t_{1/2}$ mutant = 22.6 ± 0.8 s). Thus, dimer formation is not essential for efficient FAD photoreduction under naturalistic sunlight conditions. This would allow sunlight photoreduction to continue to completion, even if sunlight-induced dimer dissociation should occur early in the photoreduction process. However, wildtype PdLCry had a slightly slower dark recovery rate than monomeric PdLCry^{E249R,T253R} (average $t_{1/2}$ wildtype = 185.2 ± 8.8 s; $t_{1/2}$ mutant = 156.7 ± 1.1 s) (Fig. 7e, f).

Discussion

Our work confirms that PdLCry from the marine bristle worm *Platynereis dumerilii* is indeed able to form dimers, as previously proposed^{22,24}, and reveals a dimerization interface centered on helix α 8 (Fig. 3), which has not been observed in CRY proteins before (Supplementary Fig. 3). While all CRY and PL proteins structurally characterized so far share the same fold and a high degree of structural similarity, it has been shown for plant CRYs that oligomerization interfaces can depend on few surface residues³⁰, complicating predictions solely based on CRY sequences. For PdLCry, we could show that dimerization depends on the presence of specific amino acids

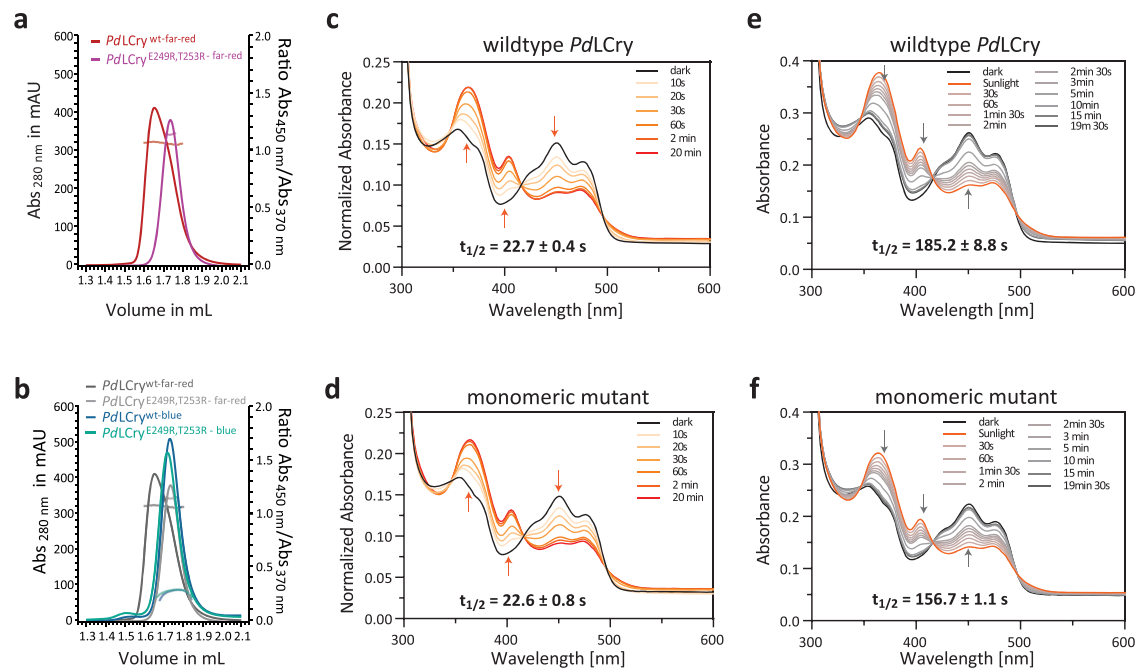


Fig. 7 | The oligomeric state of PdLCry affects its dark recovery kinetics.

a Analytical size exclusion chromatography (SEC) using a Superdex 200 Increase 5/150 GL column of PdLCry (red) and PdLCry^{E249R,T253R} (magenta) under far-red light conditions. The chromatography trace shows that the double mutation in the interface helix $\alpha 8$ quantitatively converts the dimer into a smaller species, without affecting the ground state of the chromophore that is kept in the FAD^{OX} state as indicated by the nearly equal absorbance at 370 nm and 450 nm for both wildtype and the double mutation (PdLCry red, Abs_{450nm}/Abs_{370nm} = 1.06; PdLCry^{E249R,T253R} magenta, Abs_{450nm}/Abs_{370nm} = 1.14). **b** Upon analytical SEC under continuous blue light conditions, wildtype PdLCry and PdLCry^{E249R,T253R} (dark and light blue) elute at the same volume, which coincides with the smaller species observed under far-red light conditions (light gray) for PdLCry^{E249R,T253R}, supporting the constitutively monomeric state of PdLCry^{E249R,T253R}. The dominant absorption at 370 nm compared to 450 nm (PdLCry blue, Abs_{450nm}/Abs_{370nm} = 0.28; PdLCry^{E249R,T253R} cyan, Abs_{450nm}/Abs_{370nm} = 0.28) highlights that the double mutation does not impact the ability of

PdLCry to be converted into an FAD^{ASQ}-bound photoactivated state by prolonged illumination. **c, d** Normalized absorption spectra for sunlight photoreduction on ice show that **c** wildtype PdLCry and **d** monomeric PdLCry^{E249R,T253R} have similar sunlight photoreduction rates of $t_{1/2}$ 22.7 and 22.6 s. Arrows indicate absorbance changes at 370 nm, 404 nm and 450 nm upon photoreduction of dark-state FAD^{OX} (black) to the anionic FAD^{ASQ} radical (dark orange). **e, f** Absorption spectra for dark recovery at 18 °C after full (20 min) sunlight photoreduction show that compared to **e** wildtype PdLCry, the **f** monomeric PdLCry^{E249R,T253R} mutant has a faster dark recovery with an average $t_{1/2}$ of 157 s instead of 185 s. Arrows indicate absorbance changes at 370 nm, 404 nm and 450 nm upon dark recovery of the anionic FAD^{ASQ} radical (orange) to FAD^{OX} (black). The full spectra show a representative of three independent replicates. The $t_{1/2}$ values are the means of three independent measurements with standard error of the mean (SEM). See Supplementary Fig. 7b, c for average data plots.

within helix $\alpha 8$, and that single mutations such as E249R or T253R can be sufficient to disrupt the dimer (Fig. 6a). Moreover, we found that the unique Tyr266 of the PBL, which in other animal and animal-like CRYs is usually replaced by a phenylalanine, is important for stabilizing the dimer (Fig. 6c). The importance of both Glu249 and Tyr266 is further highlighted by our MD simulation of hydrogen bonds stabilizing the dimer interface (Supplementary Fig. 3f). The unique dimer architecture of PdLCry places the PBL at a focal point connecting the chromophore, the dimer interface helix $\alpha 8$, and the CTT (Fig. 4c, d). The PBL has been identified by proteolysis experiments as a structural element affected by illumination of the chromophore in both type I⁰ and type IV CRY¹¹ proteins. For the type IV CRY C/Cry4, molecular dynamics simulations have confirmed that the PBL exhibits stronger mobility upon excitation of the chromophore³¹. In the context of our structural data, it is easy to imagine that a higher mobility of the PBL would affect the positioning of the dimer interface residue Tyr266, which is part of this loop. Furthermore, in the dark state, we observe that Pro274 and Gln271 of the PBL interact with Trp545 of the CTT, likely stabilizing this helix in its binding pocket (Fig. 4d). Indeed, our mutagenesis experiments strongly suggest that the PBL is functionally linked to both the dimer interface and the CTT (Fig. 6b, c). In addition, our PdLCry structure reveals that the FFW motif of the CTT is not invariant in type I CRYs as previously hypothesized¹⁴, with PdLCry having a cysteine instead of a phenylalanine as the middle residue without affecting positioning or anchoring of the CTT (Fig. 4c, d).

Due to its role as a light-signal gatekeeper for the circalunar clock that controls the spawning behavior of *Platynereis dumerilii*^{24,32}, PdLCry must be able to respond to dim light conditions. Indeed, in vitro experiments confirmed that PdLCry, but not its ortholog DmCry, is photoreduced by a light source that mimics underwater moonlight illumination²⁴. Our molecular structure suggests that, unlike DmCry, PdLCry has an extended electron transport chain with Tyr352 as a fifth, highly surface-exposed, member (Fig. 4b). In the avian CRY protein C/Cry4 the corresponding Tyr319 has been shown to confer an unusually high quantum yield to the protein¹¹. We showed that Tyr352 also enhances the photoresponse of PdLCry to naturalistic sunlight as its mutation leads to a less efficient FAD photoreduction under sunlight illumination (Supplementary Fig. 4a–c). This effect is potentially due to a lower quantum efficiency for FAD photoreduction in the mutants, consistent with a role of Tyr352 in electron transport to the FAD chromophore.

Interestingly, sunlight and moonlight illumination lead to different photoreduced states of PdLCry in in vitro experiments²², suggesting that the protein is able to distinguish between intensive and dim illumination as required for its in vivo activity²⁴. Our current work confirms that PdLCry can indeed form a stable dimer at dark conditions with the chromophore FAD in the resting oxidized state FAD^{OX} (Fig. 2). Based on the intense illumination conditions employed during our sample preparation, we hypothesize that the monomeric state we observe with fully reduced FAD^{ASQ} (Fig. 5)

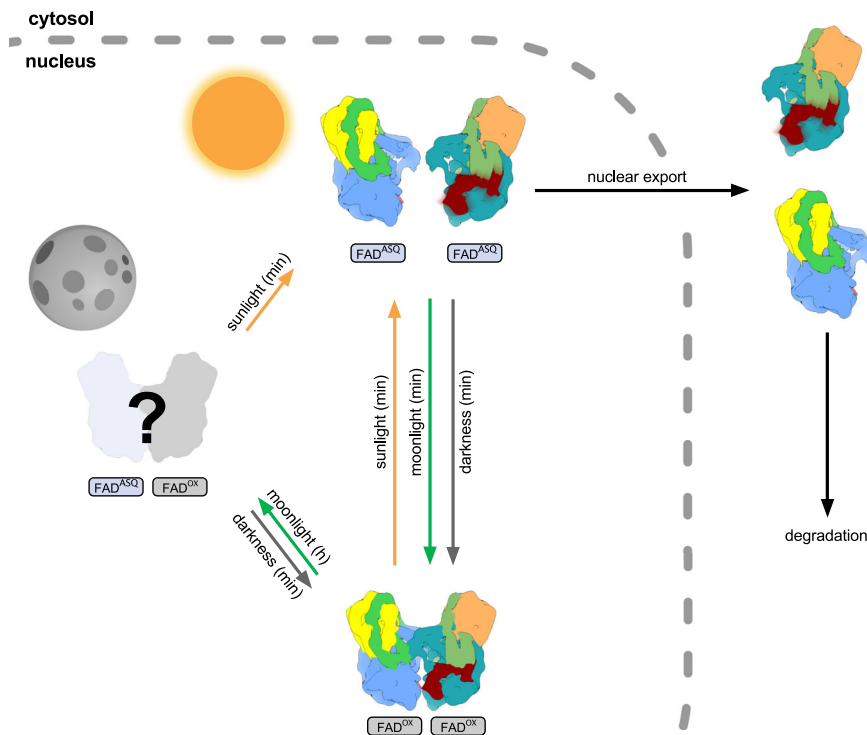


Fig. 8 | The blue light stimulated dimer-to-monomer transition rationalizes previous *in vitro* and *in vivo* data. Schematic overview of putative activation pathways at either low photon flux rates (moonlight) leading to a partial activation of the dimer within hours, or at high photon flux rates (sunlight) leading to a monomerization of the sample. *In vitro* assays have shown that the sunlight-

activated state cannot be directly converted to the moonlight-activated state²², but is only accessible via the dimeric dark state with FAD^{OX} bound in both subunits. The monomeric FAD^{ASQ}-bound state could be transported from the nucleus to the cytoplasm and subsequently targeted by a degradation pathway²⁴.

corresponds to the sunlight activated state rather than to the moonlight state.

In vitro experiments have shown that moonlight-mimicking low photon flux rates are only able to photoreduce half of the FAD present in a *PdLCry* sample, even after hours of illumination, while higher flux rates lead to a full conversion of FAD within minutes²². However, it remains to be clarified whether the partially photoreduced moonlight-state consists of *PdLCry* dimers with one oxidized and one photo-reduced FAD chromophore or of a mixture of oxidized and photo-reduced *PdLCry* monomers. Our data suggests that structural elements linking the chromophore to the dimer interface, such as the PBL, could hypothetically allow the relay of information between both chromophores, inducing an asymmetry in *PdLCry*. If thus activation of one chromophore leads to the dampening of the second chromophore, a stably half-activated moonlight state would be easy to reconcile at low photon flux rates. High flux rates however would overcome the dampening of the second chromophore, resulting in the formation of monomeric *PdLCry* as observed in our experiments (Fig. 5). Such an asymmetric, activation-rate dependent input differentiation has also been observed in the rod photoactivation cascade, allowing the dimeric photoreceptor phosphodiesterase 6 (PDE6) to differentiate thermal noise from actual photon-detection³³.

Moreover, functional assays showed that while the moonlight-induced state can be converted to the sunlight-induced state, the sunlight-induced state cannot be directly converted to the moonlight-induced state²². Our finding that *PdLCry* features an inverse photooligomerization mechanism rationalizes this observation: For conversion to the sunlight state, a partially activated moonlight state of *PdLCry*, possibly an asymmetric dimer, simply requires higher photon flux rates to activate both subunits simultaneously, leading to the dissociation of the dimer in the sunlight state. Reassembly of the dimeric state, which we propose to be necessary for the transition

from the monomeric sunlight state to the half-reduced moonlight state, may only be possible after FAD has returned to the resting state FAD^{OX}, available only by transition through the dark state (Fig. 8). Our proposed activation scheme would also explain the different dark recovery rates observed for wildtype *PdLCry* and the monomeric mutant *PdLCry*^{E249R/T253R} in our time-resolved spectroscopy experiments (Fig. 7): while we monitored the sunlight state to dark state transition - thus from monomer to dimer - for the wildtype protein, the recovery measured for *PdLCry*^{E249R/T253R} was from the monomeric sunlight state to an artificial monomeric dark state.

The shift from a dimeric to a monomeric protein population only at high photon flux rates could also explain the different cellular localization observed for *PdLCry* depending on the illumination conditions²⁴, assuming that only the monomer is targeted for nuclear export. Monomerization, nuclear export and subsequent cytosolic degradation could thus prevent erroneous activation of downstream signaling pathways by sunlight and allow input signal differentiation on the physiological level.

Methods

Sequence alignment and evolutionary analysis

The evolutionary analysis of the cryptochrome family was based on a maximum likelihood approach implemented in MEGA11 (version 11.0.10 build 211109)³⁴. For this the evolutionary history was inferred by using the maximum likelihood method and the Jones-Taylor-Thornton (JTT) matrix-based model³⁵. The bootstrap consensus tree inferred from 100 replicates³⁶ was taken to represent the evolutionary history of the taxa analyzed. Branches corresponding to partitions reproduced in less than 50% bootstrap replicates were collapsed. Initial trees for the heuristic search were obtained automatically by applying Neighbour-Join (NJ) and BioNJ algorithms to a matrix of pairwise distances estimated using the JTT model, and then selecting the topology

with superior log likelihood value. A discrete Gamma distribution was used to model evolutionary rate differences among sites (5 categories (+G, parameter = 0.8230)). This analysis involved 38 amino acid sequences, and there were a total of 1112 positions in the final dataset. For the list of used sequences see Supplementary Table 1.

Detailed pair-wise sequence alignments were calculated in Jalview (version 2.11)³⁷, relying on the JABAWS 2.2 web service³⁸ to run the Clustal Omega alignment method³⁹.

Cloning, expression and purification of PdLCry

Full-length N-terminally His6-tagged *Platynereis dumerilii* PdLCry (GenBank UUF95169) was heterologously expressed in *Spodoptera frugiperda* (Sf9, Thermo Fisher Scientific Cat No. 11496015) insect cells using the Bac-to-Bac baculovirus expression system with the pCoofy27 expression vector, as described in Poehn et al.²². Sf9 cells were grown as suspension cultures in Sf-900 SFM III media (Thermo Fisher Scientific) at 27 °C, 90 rpm. 1 L of 1×10^6 Sf9 cells mL^{-1} were transfected with P1 virus stock and incubated at 27 °C for 72 h. Cells were harvested by centrifugation at $10,000 \times g$ for 20 min and stored at -80 °C until purification. All purification steps were carried out in dark or dim red light conditions. Columns were wrapped with aluminum foil to avoid light-activation of PdLCry. The cell pellets were resuspended in lysis buffer (20 mM Tris pH 7.5, 150 mM NaCl, 20 mM imidazole, 5% glycerol, 5 mM β -mercaptoethanol) and lysed using a Branson sonifier (Analog Sonifier 450-CE). The lysate was centrifuged at $50,000 \times g$ for 45 min. The clarified supernatant was loaded onto a HisTrap FF crude 5 mL column (Cytiva), and PdLCry was eluted in a 20 mM to 1000 mM imidazole gradient. Elution fractions containing PdLCry were concentrated, diluted with no-salt buffer (50 mM Tris pH 7.5, 5% glycerol, 1 mM DTT) and loaded onto a 5 mL Hitrap Q HP anion exchange column (Cytiva). A gradient from 0% to 100% high salt buffer (50 mM Tris pH 7.5, 1 M NaCl, 5% glycerol, 1 mM DTT) was applied. PdLCry containing fractions were pooled, concentrated and loaded onto a Superdex S200 10/300 GL or a HiLoad S200 16/60 SEC column (buffer 25 mM Bis-tris propane pH 8.0, 150 mM NaCl, 5% glycerol, 1 mM TCEP). Fractions containing pure PdLCry were pooled, concentrated to 10 mg mL^{-1} and snap frozen in liquid nitrogen for storage at -80 °C.

Site-directed mutagenesis, expression, and purification of PdLCry mutants

PdLCry mutants were generated by QuikChange (Agilent) site-directed mutagenesis and verified by sequencing. The mutant constructs were expressed and purified essentially as described for wildtype PdLCry.

Cryo-EM sample preparation and data collection

All samples for cryo-EM were prepared in a dark lab under far-red light illumination (Osram OSLOM SSL 120, GF CSSPM1.24). Concentrated samples of dark-adapted PdLCry were diluted to a concentration of 0.7 mg mL^{-1} using glycerol-free SEC buffer (25 mM Bis-tris propane pH 8.0, 150 mM NaCl, 1 mM TCEP). Dark-adapted samples were additionally supplemented with 0.01% fluorinated octyl maltoside (fOM). 4.5 μL of the mixture were then applied on either a glow-discharged Ultra-Ufoil R1.2/1.3 Au300 or a Quantifoil R1.2/1.3 Cu300 grid (Quantifoil Micro Tools GmbH), blotted for 3 sec and flash-frozen in liquid ethane using a Vitrobot Mark IV device (Thermo Fisher Scientific) set to 100% humidity at 21 °C. Grids were stored under liquid nitrogen conditions until usage. For blue light activation, grids were illuminated for 30 secs in the humidifier chamber of the freeze-plunger using a 455 nm blue light LED (Thorlabs M455L4, operated at 1000 mA). To ensure optimal illumination, a liquid-light guide (Thorlabs LLG03-4H) was used to bring the light source within 3 mm of the grid surface. Cryo-EM data was acquired using a Titan Krios G3i (Thermo Fisher Scientific) electron microscope operated at 300 kV. Images were collected automatically using EPU (version 2.12) (Thermo Fisher Scientific) on a Falcon III direct electron detector with a calibrated pixel size of

$0.862 \text{ \AA px}^{-1}$. For the dark state, movies were either acquired in integration mode using a total dose of $66 \text{ e}^- \text{ \AA}^{-2}$ distributed among 19 frames, or in counting mode with a total dose of $27 \text{ e}^- \text{ \AA}^{-2}$ distributed among either 24 or 48 frames. For the blue light state, movies were acquired in counting mode with a total dose of $30 \text{ e}^- \text{ \AA}^{-2}$ distributed among 36 frames. Defocus values ranged from -0.3 to $-2.0 \mu\text{m}$.

Image processing, quantification of monomer-to-dimer distribution, and model building

Image processing was performed using cryoSPARC (version 3.3.2+patch 220518)⁴⁰. Movie stacks were first corrected for drift and beam-induction motion, and then used to determine defocus and other CTF-related values. Only high-quality micrographs with low drift metrics, low astigmatism and good agreement between experimental and calculated CTFs were further processed. On these high-quality micrographs putative particles were automatically picked based on expected protein diameter, extracted, and subjected to reference-free 2D classification. Based on this classification result, we estimated the number of particles showing either a monomer, a dimer or an ambiguous assembly - excluding classes showing clear artefacts. Representative 2D classes were then used for a template-based picking approach, particles extracted again, subjected to reference-free 2D classification to exclude artefacts, and subsequent 3D classification using C1 symmetry to identify high-quality particles. 3D classification was performed with a target resolution of 6 \AA in order to ensure that secondary-structure elements are also included as a feature in the classification algorithm. Particles showing protein-like density features, especially features resembling secondary structure elements, were further refined using the non-uniform refinement strategy. For the dark state sample, C2 symmetry was enforced yielding a map at a global resolution of 2.6 \AA . For the blue light-activated sample C1 refinement yielded a map at a nominal global resolution of 3.5 \AA that was strongly anisotropic and thus filtered to 8 \AA for further interpretation. For further details see Supplementary Fig. 2 and 5, and Supplementary Table 2.

The atomic model was built starting from the *DmCry* crystal structure (PDB ID 4JZY) and the PdLCry amino acid sequence (GenBank UUF951691). First, Coot (version 0.9.4.7)⁴¹ was used to semi-manually fit amino acids into a single subunit of the EM density map. Next, Phenix (version 1.20)⁴² was used to generate a non-crystallographic symmetry (NCS)-related second subunit and both subunits were then simultaneously refined against the 3D density map. This process was iterated until the fit to the density map and geometric parameters converged. The final atomic model accounts for residues 31 to 556. For further details and statistics see Supplementary Table 2. Molecular visualization and analysis were done using UCSF ChimeraX (version 1.5)⁴³.

MD simulations

The PdLCry structure used for simulations was from this study. The structures for *Arabidopsis thaliana* Cry2 (AtCry2, PDB ID: 6K8I) and *Drosophila melanogaster* Cry (DmCry, PDB ID: 4JZY) were taken from the PDB database. The experimentally unresolved parts of AtCry2 were reconstructed using AlphaFold^{44,45}, where the AtCry2 sequence was used as an input. A root mean square deviation (RMSD) comparison of the backbone atoms between the AlphaFold generated AtCry2 monomeric structure and the PDB structure showed a difference of 1.8 \AA .

Altogether 4 molecular dynamics (MD) simulations were performed using NAMD (version 2.14)⁴⁶⁻⁴⁸ interfaced through the VIKING platform⁴⁹. Two replica simulations of PdLCry were carried out for 190 ns, while AtCry2 and DmCry were simulated once for 190 ns. All simulations initially included 10,000 conjugate gradient minimization steps. The simulations were then split into four distinct stages, first three used to equilibrate the system, and the fourth stage being used

for analysis (production simulation). The first three equilibration simulations were completed in an isothermal-isobaric (NPT) ensemble, while production simulations assumed a canonical (NVT) statistical ensemble. The three equilibration stages were carried out for 1 ns, 2 ns, and 2 ns, respectively, assuming different constraints in the system. In the first stage, the entire protein and FAD were harmonically constrained to the atomic positions taken from the experimental structure. In the second equilibration stage, the backbone atoms continued being constrained, while the side-chain atoms were free to move. The final equilibration stage continued with all atoms being free to move. Each production simulation was carried out over 190 ns with an integration time step of 2 fs, assuming the hydrogen atoms to be rigidly bonded to the corresponding heavier atoms. All simulations (equilibration and production) assumed a temperature of 310 K, controlled through the Langevin thermostat and an atmospheric pressure of 1 bar maintained through the Nosé–Hoover barostat. CHARMM36 force field with CMAP corrections was used in all simulations^{50–55}. The investigated *PdL*Cry was set to be in the inactive state that is usually present in dark conditions, where the FAD cofactor is fully oxidized. Simulation parameters for the FAD cofactor were adopted from earlier studies^{31,56–60}. NaCl was used to neutralize the total charge of the system and assumed at a concentration of 0.15 mol L⁻¹ in all simulations. Van der Waals and electrostatic interactions were treated with the cut-off distances of 12 Å, while the particle-mesh Ewald (PME) summation method was used to treat the long-range electrostatic interactions⁶¹. The size of the simulation box for *At*Cry2 was 102 Å × 136 Å × 140 Å and contained 201,877 atoms, for *Dm*Cry the simulation box was 134 Å × 105 Å × 135 Å with 199,362 atoms, and for *PdL*Cry the simulation box was 111 Å × 118 Å × 109 Å, containing 148,535 atoms.

Convergence was assessed by following the RMSD evolution over time, with the RMSD defined as follows:

$$RMSD(t) = \sqrt{\frac{1}{N} \sum_{i=1}^N |\vec{r}_i(t) - \vec{r}_i^{ref}|^2} \quad (1)$$

where N is the number of backbone atoms in a given dimer, $\vec{r}_i(t)$ is the position vector of the i th atom at a time instance, t , and \vec{r}_i^{ref} is the position vector of the i th atom at the reference time point. To analyze the buried area of the dimeric cryptochrome structures, the difference between the solvent accessible surface area (SASA) was computed as:

$$S_0 = (S_1 + S_2) - S_d \quad (2)$$

Here S_0 is the interaction surface (or the buried area) between the monomers in a dimer, S_1 and S_2 are the SASAs of the two monomers and S_d is the SASA value of the whole dimer. The SASA maximal speed molecular surfaces (MSMS) algorithm⁶² in VMD⁶³ was used to compute the values in Eq. (1), assuming each atom having a radius of 1.4 Å. Hydrogen bond analysis was performed using the HBonds plugin in VMD (version 1.9.3)⁶³.

Analytical SEC and inline UV/Vis spectroscopy

For inline UV/Vis spectroscopy analytical SEC runs were performed in a dark lab under far-red light illumination (Osram OSRON SSL 120, GF CSSPML.24) using a Superdex 200 Increase 5/150 GL (Cytiva) SEC column connected to an bioinert AZURA HPLC system (Knauer) equipped with an autosampler and a TIR multiwavelength detector set to measure absorption at 280 nm, 370 nm, 404 nm and 450 nm. Data collection was controlled using the PurityChrom (version 5.09.115) software. The flow rate for all runs was 0.16 mL min⁻¹. Concentrated samples of dark-adapted *PdL*Cry were diluted to a concentration of 5 mg mL⁻¹ using a buffer containing 25 mM Bis-tris propane (pH 8.0), 150 mM NaCl, and 1 mM TCEP, prior to injection of 7 μL per run. For dark condition runs, the chromatography column was wrapped in

aluminum foil. For blue light condition runs, samples were pre-activated for 60 sec using a 455 nm blue light LED (Thorlabs M455L4, operated at 1000 mA) at a distance of 1 cm. During the run, the chromatography column was continuously illuminated by a 451 nm blue light LED array (24x Osram OSRON SSL 120, GF CSSPML.14) installed at a distance of 10 cm in parallel to the column and reflected by mirror elements.

Analytical SEC runs without inline UV/Vis spectroscopy were carried out under far-red light conditions using a Superdex 200 10/300 GL column wrapped in aluminum foil connected to a Biorad NGC Quest10 Plus Chromatography System. For each SEC run, 100 μL sample diluted to a concentration of 2 mg mL⁻¹ concentration was injected. Data collection was controlled using the ChromLab (version 6.1) software.

UV/Vis spectroscopic analyses of blue light and sunlight photoreduction and dark recovery

UV/Visible absorption spectra of the purified *PdL*Cry proteins in final SEC purification buffer (25 mM Bis-tris propane pH 8.0, 150 mM NaCl, 5% glycerol, 1 mM TCEP), supplemented with 1 mM DTT, were recorded on a Tecan Spark 20M plate reader using the Spark Control (version 2.2) software. A light state spectrum of *PdL*Cry with fully photoreduced FAD^{AsQ} was collected after illuminating dark-adapted *PdL*Cry for 2 min with a 450 nm blue LED (41 W m⁻² at sample). To analyze sunlight dependent FAD photoreduction kinetics, dark-adapted *PdL*Cry was illuminated with naturalistic sunlight (Marine Breeding Systems GmbH²²) with 4.6 W m⁻² intensity at the sample for up to 20 min (protein kept on ice) and complete UV–VIS spectra (300–700 nm) were collected after different time intervals. Sunlight photoreduction kinetics (on ice) were determined based on changes of 450 nm absorbance values, that were extracted from these UV/VIS spectra after normalization to their isosbestic point at 416 nm. Normalization of sunlight photoreduction experiments was required to correct for baseline shifts caused by sample handling at each measurement time point, and (in the case of kinetic studies) because two additional samples had to be measured to determine FAD photoreduction after 10 s and 20 s sunlight illumination. Dark recovery kinetics (FAD reoxidation) after photoreduction by 20 min sunlight illumination were determined at 18 °C by recording absorbance changes at 450 nm.

Absorption spectra and kinetics were analyzed using GraphPad PRISM (version 9.5.1-733). The half-life time values ($t_{1/2}$ [s]) for dark recovery and photoreduction kinetics were calculated by fitting a single exponential curve to the experimental data. The single exponential model is described as $Y = (Y_0 - Y_{plateau})e^{-KX} + Y_{plateau}$, where Y_0 and $Y_{plateau}$ correspond to the 450 nm absorbance values at the start and end points of the measurement, K represents the rate constant [s⁻¹] and the half-life time $t_{1/2} = \ln(2) * K^{-1}$ [s]. The standard error of the mean (SEM) was used to describe the error of the measurements and of the $t_{1/2}$ values. $SEM = \frac{SD}{\sqrt{n}}$ where SD is the standard deviation and n is the number of replicates.

Reporting summary

Further information on research design is available in the Nature Portfolio Reporting Summary linked to this article.

Data availability

The EM maps for the dark state and blue light activated state have been deposited in the EMDB under accession codes [EMD-17429](https://doi.org/10.1038/EMD-17429) and [EMD-17553](https://doi.org/10.1038/EMD-17553). The raw electron microscopy data are available on request due to their large size. Atomic coordinates for dark state *PdL*Cry have been deposited in the Protein Data Bank under the accession code [PDB 8P4X](https://doi.org/10.1038/PDB-8P4X). The sequence analysis data, SEC data, MD data, and UV/Vis data have been deposited in the Zenodo repository under the <https://doi.org/10.5281/zenodo.8420035>.

References

- Chaves, I. et al. The cryptochromes: blue light photoreceptors in plants and animals. *Annu. Rev. Plant Biol.* **62**, 335–364 (2011).
- Michael, A. K., Fribourgh, J. L., Van Gelder, R. N. & Partch, C. L. Animal cryptochromes: divergent roles in light perception, circadian timekeeping and beyond. *Photochem. Photobiol.* **93**, 128–140 (2017).
- Wang, Q. & Lin, C. Mechanisms of cryptochrome-mediated photoresponses in plants. *Annu. Rev. Plant Biol.* **71**, 103–129 (2020).
- Öztürk, N. et al. Structure and function of animal cryptochromes. *Cold Spring Harb. Symp. Quant. Biol.* **72**, 119–131 (2007).
- Sancar, A. Structure and function of DNA photolyase and cryptochrome blue-light photoreceptors. *Chem. Rev.* **103**, 2203–2237 (2003).
- Bartölke, R. et al. The secrets of cryptochromes: photoreceptors, clock proteins, and magnetic sensors. *Neuroforum* **27**, 151–157 (2021).
- Karki, N., Vergish, S. & Zoltowski, B. D. Cryptochromes: photochemical and structural insight into magnetoreception. *Protein Sci.* **30**, 1521–1534 (2021).
- Oztürk, N., Selby, C. P., Annayev, Y., Zhong, D. & Sancar, A. Reaction mechanism of *Drosophila* cryptochrome. *Proc. Natl Acad. Sci.* **108**, 516–521 (2011).
- Czarna, A. et al. Structures of *Drosophila* cryptochrome and mouse cryptochrome1 provide insight into circadian function. *Cell* **153**, 1394–1405 (2013).
- Vaidya, A. T. et al. Flavin reduction activates *Drosophila* cryptochrome. *Proc. Natl Acad. Sci.* **110**, 20455–20460 (2013).
- Zoltowski, B. D. et al. Chemical and structural analysis of a photoactive vertebrate cryptochrome from pigeon. *Proc. Natl Acad. Sci.* **116**, 19449–19457 (2019).
- Partch, C. L., Clarkson, M. W., Özgür, S., Lee, A. L. & Sancar, A. Role of structural plasticity in signal transduction by the cryptochrome blue-light photoreceptor. *Biochemistry* **44**, 3795–3805 (2005).
- Berntsson, O. et al. Photoactivation of *Drosophila melanogaster* cryptochrome through sequential conformational transitions. *Sci. Adv.* **5**, eaaw1531 (2019).
- Zoltowski, B. D. et al. Structure of full-length *Drosophila* cryptochrome. *Nature* **480**, 396–399 (2011).
- Schleicher, E. et al. Electron nuclear double resonance differentiates complementary roles for active site histidines in (6-4) photolyase. *J. Biol. Chem.* **282**, 4738–4747 (2007).
- Ganguly, A. et al. Changes in active site histidine hydrogen bonding trigger cryptochrome activation. *Proc. Natl Acad. Sci.* **113**, 10073–10078 (2016).
- Chandrasekaran, S. et al. Tuning flavin environment to detect and control light-induced conformational switching in *Drosophila* cryptochrome. *Commun. Biol.* **4**, 249 (2021).
- Ponnu, J. & Hoecker, U. Signaling mechanisms by Arabidopsis cryptochromes. *Front. Plant Sci.* **13**, 844714 (2022).
- Parico, G. C. G. & Partch, C. L. The tail of cryptochromes: an intrinsically disordered cog within the mammalian circadian clock. *Cell Commun. Signal.* **18**, 182 (2020).
- Oldemeyer, S. et al. Essential role of an unusually long-lived tyrosyl radical in the response to red light of the animal-like cryptochrome aCRY. *J. Biol. Chem.* **291**, 14062–14071 (2016).
- Franz-Badur, S. et al. Structural changes within the bifunctional cryptochrome/photolyase CraCRY upon blue light excitation. *Sci. Rep.* **9**, 9896 (2019).
- Poehn, B. et al. A Cryptochrome adopts distinct moon- and sunlight states and functions as sun- versus moonlight interpreter in monthly oscillator entrainment. *Nat. Commun.* **13**, 5220 (2022).
- Özpolat, B. D. et al. The Nereid on the rise: Platynereis as a model system. *EvoDevo* **12**, 10 (2021).
- Zurl, M. et al. Two light sensors decode moonlight versus sunlight to adjust a plastic circadian/circalunidian clock to moon phase. *Proc. Natl Acad. Sci.* **119**, e2115725119 (2022).
- Oliveri, P. et al. The cryptochrome/photolyase Family in aquatic organisms. *Mar. Genomics* **14**, 23–37 (2014).
- Liu, B., Liu, H., Zhong, D. & Lin, C. Searching for a photocycle of the cryptochrome photoreceptors. *Curr. Opin. Plant Biol.* **13**, 578–586 (2010).
- Franz, S. et al. Structure of the bifunctional cryptochrome aCRY from *Chlamydomonas reinhardtii*. *Nucleic Acids Res.* **46**, 8010–8022 (2018).
- Wang, Y., Veglia, G., Zhong, D. & Gao, J. Activation mechanism of *Drosophila* cryptochrome through an allosteric switch. *Sci. Adv.* **7**, eabg3815 (2021).
- Berndt, A. et al. A novel photoreaction mechanism for the circadian blue light photoreceptor *Drosophila* cryptochrome. *J. Biol. Chem.* **282**, 13011–13021 (2007).
- Shao, K. et al. The oligomeric structures of plant cryptochromes. *Nat. Struct. Mol. Biol.* **27**, 480–488 (2020).
- Schuhmann, F., Kattnig, D. R. & Solov'yov, I. A. Exploring post-activation conformational changes in pigeon cryptochrome 4. *J. Phys. Chem. B* **125**, 9652–9659 (2021).
- Zantke, J. et al. Circadian and circalunar clock interactions in a marine annelid. *Cell Rep.* **5**, 99–113 (2013).
- Qureshi, B. M. et al. It takes two transducins to activate the cGMP-phosphodiesterase 6 in retinal rods. *Open Biol.* **8**, 180075 (2018).
- Tamura, K., Stecher, G. & Kumar, S. MEGA11: molecular evolutionary genetics analysis Version 11. *Mol. Biol. Evol.* **38**, 3022–3027 (2021).
- Jones, D. T., Taylor, W. R. & Thornton, J. M. The rapid generation of mutation data matrices from protein sequences. *Bioinformatics* **8**, 275–282 (1992).
- Felsenstein, J. Confidence limits on phylogenies: an approach using the bootstrap. *Evolution* **39**, 783–791 (1985).
- Waterhouse, A. M., Procter, J. B., Martin, D. M. A., Clamp, M. & Barton, G. J. Jalview Version 2-A multiple sequence alignment editor and analysis workbench. *Bioinformatics* **25**, 1189–1191 (2009).
- Troshin, P. V. et al. JABAWS 2.2 distributed web services for Bioinformatics: protein disorder, conservation and RNA secondary structure. *Bioinformatics* **34**, 1939–1940 (2018).
- Sievers, F. et al. Fast, scalable generation of high-quality protein multiple sequence alignments using Clustal Omega. *Mol. Syst. Biol.* **7**, 539 (2011).
- Punjani, A., Rubinstein, J. L., Fleet, D. J. & Brubaker, M. A. CryoSPARC: algorithms for rapid unsupervised cryo-EM structure determination. *Nat. Methods* **14**, 290–296 (2017).
- Emsley, P., Lohkamp, B., Scott, W. G. & Cowtan, K. Features and development of Coot. *Acta Crystallogr. D: Biol. Crystallogr.* **66**, 486–501 (2010).
- Adams, P. D. et al. PHENIX: a comprehensive Python-based system for macromolecular structure solution. *Acta Crystallogr. D: Biol. Crystallogr.* **66**, 213–221 (2010).
- Pettersen, E. F. et al. scp>UCSF ChimeraX</scp>: structure visualization for researchers, educators, and developers. *P.rotein Sci.* **30**, 70–82 (2021).
- Jumper, J. et al. Highly accurate protein structure prediction with AlphaFold. *Nature* **596**, 583–589 (2021).
- Varadi, M. et al. AlphaFold Protein Structure Database: massively expanding the structural coverage of protein-sequence space with high-accuracy models. *Nucleic Acids Res.* **50**, D439–D444 (2022).
- Kalé, L. et al. NAMD2: greater scalability for parallel molecular dynamics. *J. Comput. Phys.* **151**, 283–312 (1999).
- Phillips, J. C. et al. Scalable molecular dynamics with NAMD. *J. Comput. Chem.* **26**, 1781–1802 (2005).
- Phillips, J. C. et al. Scalable molecular dynamics on CPU and GPU architectures with NAMD. *J. Chem. Phys.* **153**, 044130 (2020).

49. Korol, V. et al. Introducing VIKING: a novel online platform for multiscale modeling. *ACS Omega* **5**, 1254–1260 (2020).
50. Foloppe, N. & Mackerell, A. D. Jr All-atom empirical force field for nucleic acids: I. Parameter optimization based on small molecule and condensed phase macromolecular target data. *J. Comput. Chem.* **21**, 86–104 (2000).
51. Hart, K. et al. Optimization of the CHARMM additive force field for DNA: improved treatment of the BI/BII conformational equilibrium. *J. Chem. Theory Comput.* **8**, 348–362 (2012).
52. Huang, J. & Mackerell, A. D. CHARMM36 all-atom additive protein force field: Validation based on comparison to NMR data. *J. Comput. Chem.* **34**, 2135–2145 (2013).
53. Buck, M., Bouguet-Bonnet, S., Pastor, R. W. & Mackerell, A. D. Importance of the CMAP correction to the CHARMM22 protein force field: dynamics of hen lysozyme. *Biophys. J.* **90**, L36–L38 (2006).
54. Best, R. B. et al. Optimization of the additive CHARMM all-atom protein force field targeting improved sampling of the backbone ϕ , ψ and side-chain χ_1 and χ_2 dihedral angles. *J. Chem. Theory Comput.* **8**, 3257–3273 (2012).
55. Denning, E. J., Priyakumar, U. D., Nilsson, L. & Mackerell, A. D. Impact of 2'-hydroxyl sampling on the conformational properties of RNA: Update of the CHARMM all-atom additive force field for RNA. *J. Comput. Chem.* **32**, 1929–1943 (2011).
56. Xu, J. et al. Magnetic sensitivity of cryptochrome 4 from a migratory songbird. *Nature* **594**, 535–540 (2021).
57. Lüdemann, G., Solov'yov, I. A., Kubař, T. & Elstner, M. Solvent driving force ensures fast formation of a persistent and well-separated radical pair in plant cryptochrome. *J. Am. Chem. Soc.* **137**, 1147–1156 (2015).
58. Solov'yov, I. A., Domratcheva, T., Moughal Shahi, A. R. & Schulten, K. Decrypting cryptochrome: revealing the molecular identity of the photoactivation reaction. *J. Am. Chem. Soc.* **134**, 18046–18052 (2012).
59. Sjulstok, E., Solov'yov, I. A. & Freddolino, P. L. In *Methods in Enzymology* Vol. 620, 277–314 (Elsevier, 2019).
60. Hanić, M. et al. Computational reconstruction and analysis of structural models of avian cryptochrome 4. *J. Phys. Chem. B* **126**, 4623–4635 (2022).
61. Darden, T., York, D. & Pedersen, L. Particle mesh Ewald: An $N \cdot \log(N)$ method for Ewald sums in large systems. *J. Chem. Phys.* **98**, 10089–10092 (1993).
62. Sanner, M. F., Olson, A. J. & Spehner, J.-C. Reduced surface: an efficient way to compute molecular surfaces. *Biopolymers* **38**, 305–320 (1996).
63. Humphrey, W., Dalke, A. & Schulten, K. VMD: visual molecular dynamics. *J. Mol. Graph.* **14**, 33–38 (1996).

Acknowledgements

The authors thank Christoph Klatt for contributions at an early stage of the project, and acknowledge use of the ESRF beamline CM01 during an early stage of the project. We are grateful for laboratory support by Alexandra Schneider, and by the IMB Media Lab, Protein Production, and Proteomics Core Facilities. We acknowledge access to the cryo-EM infrastructure of StruBiTEM (Cologne, funded by DFG Grant INST 216/949-1 FUGG), to the computing infrastructure of CARL (Oldenburg, supported by the DFG and the Ministry for Science and Culture of Lower Saxony), and to the computing infrastructure of CHEOPS (Cologne, funded by DFG Grant INST 216/512/1 FUGG). Additional computing infrastructure was provided by the Resource Allocation Board on the supercomputer Lise and Emmy at NHR@ZIB and NHR@Göttingen under

project nip00058 (to I.A.S.) and a hardware grant from NVIDIA (to E.B.). This study was supported by funding from the DFG (SFB1372-SigO3 to E.B.; SFB1372-SigO5 to I.A.S.; GRK1885 to I.A.S.; TRR386/1-2023 HYP*-MOL, no 514664767 to I.A.S.); a DFG fellowship of the Excellence Initiative by the Graduate School Materials Science in Mainz (GSC 266, to S.K.), the Ministry for Science and Culture of Lower Saxony (SMART and DyNano to I.A.S.), and the Volkswagen Foundation (Lichtenberg Professorship to I.A.S.).

Author contributions

H.H.V., S.K., and C.H. prepared protein samples; H.H.V. carried out protein mutagenesis; H.H.V., H.B., D.D., and C.H. carried out SEC experiments; H.H.V. carried out time-resolved spectroscopy experiments; H.B. carried out sequence analysis; H.B., M.G., and G.J. prepared cryo-EM samples; M.G. and G.J. acquired cryo-EM data; H.B. and E.B. performed cryo-EM data analysis; H.B. prepared atomic models with input from E.W. and E.B.; M.H. carried out MD experiments; H.H.V., H.B., M.H., I.A.S., E.W., and E.B. interpreted data; E.B. and E.W. conceived the project; I.A.S., E.W., and E.B. supervised the project; E.B. wrote the manuscript with input from all authors.

Funding

Open Access funding enabled and organized by Projekt DEAL.

Competing interests

The authors declare no competing interests.

Additional information

Supplementary information The online version contains supplementary material available at <https://doi.org/10.1038/s41467-023-42708-2>.

Correspondence and requests for materials should be addressed to Eva Wolf or Elmar Behrmann.

Peer review information *Nature Communications* thanks Lorenzo Cupellini and the other, anonymous, reviewer(s) for their contribution to the peer review of this work. A peer review file is available.

Reprints and permissions information is available at <http://www.nature.com/reprints>

Publisher's note Springer Nature remains neutral with regard to jurisdictional claims in published maps and institutional affiliations.

Open Access This article is licensed under a Creative Commons Attribution 4.0 International License, which permits use, sharing, adaptation, distribution and reproduction in any medium or format, as long as you give appropriate credit to the original author(s) and the source, provide a link to the Creative Commons license, and indicate if changes were made. The images or other third party material in this article are included in the article's Creative Commons license, unless indicated otherwise in a credit line to the material. If material is not included in the article's Creative Commons license and your intended use is not permitted by statutory regulation or exceeds the permitted use, you will need to obtain permission directly from the copyright holder. To view a copy of this license, visit <http://creativecommons.org/licenses/by/4.0/>.

© The Author(s) 2023